New Journal of Physics
The open access journal for physics

High-resolution magnetic-domain imaging by Fourier transform holography at 21 nm wavelength

Stefan Schaffert[1], Bastian Pfau[1], Jan Geilhufe[2], Christian M Günther[1], Michael Schneider[1], Clemens von Korff Schmising[1] and Stefan Eisebitt[1,2,3]

[1] Institut für Optik und Atomare Physik, Technische Universität Berlin, Straße des 17. Juni 135, D-10623 Berlin, Germany
[2] Helmholtz-Zentrum Berlin für Materialien und Energie GmbH, Hahn-Meitner-Platz 1, D-14109 Berlin, Germany
E-mail: eisebitt@physik.tu-berlin.de

New Journal of Physics **15** (2013) 093042 (10pp)
Received 10 May 2013
Published 27 September 2013
Online at http://www.njp.org/
doi:10.1088/1367-2630/15/9/093042

Abstract. Exploiting x-ray magnetic circular dichroism at the L-edges of 3d transition metals, Fourier transform holography has become a standard technique to investigate magnetic samples with sub-100 nm spatial resolution. Here, magnetic imaging in the 21 nm wavelength regime using M-edge circular dichroism is demonstrated. Ultrafast pulses in this wavelength regime are increasingly available from both laser- and accelerator-driven soft x-ray sources. We explain the adaptations concerning sample preparation and data evaluation compared to conventional holography in the 1 nm wavelength range. We find the correction of the Fourier transform hologram to in-plane Fourier components to be critical for high-quality reconstruction and demonstrate 70 nm spatial resolution in magnetization imaging with this approach.

[3] Author to whom any correspondence should be addressed.

Content from this work may be used under the terms of the Creative Commons Attribution 3.0 licence. Any further distribution of this work must maintain attribution to the author(s) and the title of the work, journal citation and DOI.

© IOP Publishing Ltd and Deutsche Physikalische Gesellschaft

Contents

1. Introduction

In the last decade, interference-based techniques using soft and hard x-rays have been increasingly used to address imaging problems at sub-100 nm spatial resolution. One driving force for this development is the increasing availability of sources with appreciable *coherent* photon flux; a development that is fuelled both by accelerator based sources such as free-electron lasers (FELs) and high harmonic generation (HHG) sources driven by optical lasers. Fourier transform holography (FTH) allows solving the phase problem via interference with a reference wave [1, 2]. FTH at x-ray wavelengths has recently been applied to study problems in different scientific areas, with a certain emphasis on nanomagnetism [3–7]. Here, the use of x-rays which are in resonance with corresponding electronic transitions gives rise to strong magnetic contrast via x-ray magnetic circular dichroism (XMCD).

On the other hand, magnetization *dynamics* on a sub-picosecond timescale has become a very rapidly growing research area, including phenomena such as ultrafast demagnetization and switching processes [8–10]. The underlying mechanisms are under intense debate [11–14] while at the same time nanoscale structures are expected to exhibit new phenomena [15–17].

Both FELs and HHG sources deliver coherent femtosecond x-ray pulses suitable for holographic imaging with femtosecond temporal and nanometer spatial resolution [18, 19]. The generation of magnetic contrast for the most prominent and technologically relevant elements Fe, Co and Ni via XMCD requires wavelengths around 1.6 nm when operating in resonance with the L-absorption edges and around 20 nm when using resonant scattering at the M-absorption edges. So far, ultrafast imaging of magnetic nanostructures has only been performed using XMCD at the Co L_3-edge ($2p_{3/2}$) at the Linac Coherent Light Source [20]. In fact, the exploitation of soft x-rays at the Fe, Co or Ni M-edges for magnetic imaging via FTH has not yet been demonstrated at all. Given the fact that HHG sources in this wavelength range become more prolific and that two FELs worldwide are currently operating in this energy range, it seems timely to demonstrate that sub-100 nm resolution magnetic imaging via FTH is feasible in this spectral range. In this work, we demonstrate the use of 20.8 nm wavelength radiation in resonance with the Co 3p level for high-resolution imaging and describe experimental and data-treatment details insofar as they differ from the use of FTH in the 1.6 nm regime such as described in [21].

2. Experimental concepts and details

In comparison to using the L-edge resonances to image nanomagnetic structures, utilizing 3d transition metal M-edges has several implications for the experimental setup as well as

the data-treatment. In the following, we refer to the Co transition wavelengths of 20.8 nm (58.9 eV photon energy) and 1.59 nm (778 eV) as prototypical for the 3d transition metal M- and L-edges, respectively. At the M-edges opposed to the L-edges one generally observes that (i) the x-ray attenuation length is smaller, (ii) the x-ray reflectivity is higher, (iii) the *relative* XMCD contrast is comparable [22], while the *absolute* scattering cross-section is lower, and (iv) less electron–hole pairs per photon are generated in a charge-coupled device (CCD) detector.

In order to optimize scattering experiments in transmission geometry, support structures (e.g. Si_3N_4 membranes) have to be thinner to avoid unnecessary absorption. At the same time, the holographic mask can be thinner thus typically allowing for higher resolution lateral patterning at the same width/depth aspect ratio. The reduced detector counts per photon in association with small (resonant magnetic) scattering rates and higher reflectivities imply that it is more difficult to obtain the required signal to detect hologram fringes of small magnetic features. On the other hand noise due to low-energy diffuse stray light is a more severe issue as compared to experiments at the L-edges. Considering scattering from $d = 100$ nm structures we see that the corresponding scattering angles $\sin(\theta) \approx \lambda/d$ are on the order of 12° (M-edge) and 1° (L-edge), respectively, necessitating a different experimental geometry and allowing for small-angle approximations in the L-edge case. The latter are not applicable when operating in resonance with the M-edges. Finally, given these different geometries and optical constants, the influence of refraction at material and vacuum interfaces will have to be considered in the 20.8 nm wavelength case.

The experiment was carried out at the UE112-PGM1 undulator beamline at BESSY II using circularly polarized radiation tuned to the nominal Co M_3 and M_2 resonance at 20.8 nm to maximize XMCD contrast. A 200 nm Al filter upstream of the sample was used to reduce the third diffraction order radiation residually present from the undulator/monochromator. The sample consists of a magnetic domain pattern in a $[\mathrm{Co}(0.8\,\mathrm{nm})/\mathrm{Pt}(1.4\,\mathrm{nm})]_{11}$ multilayer film with perpendicular magnetic anisotropy, sputter deposited on a Si_3N_4 membrane of 30 nm thickness. A Ta(2 nm)/Pt(3 nm) seed layer was used for adhesion and an additional 0.6 nm Pt cap was deposited to prevent oxidation of the magnetic multilayer. Due to the interplay of magnetostatic energy and exchange energy, a labyrinth pattern of out-of-plane magnetized domains forms in the magnetic multilayer [23].

From magnetic force microscopy we determine an average domain periodicity of about 140 nm (not shown). To realize an FTH geometry, a gold mask is fabricated on the sample via focused ion beam lithography as described by Eisebitt *et al* [21]. Given the reduced x-ray attenuation length in Au at $\lambda = 20.8$ nm as compared to 1.59 nm, the Au mask had a thickness of 250 nm (as compared to typically 1000 nm at 1.59 nm). Multi-reference FTH imaging [24] was obtained by placing five reference holes evenly on a 5.5 μm radius around the circular object aperture, which had a diameter of 2 μm. The reference apertures had nominal diameters of 60 nm for the three apertures labelled 1, 2 and 5 in the following and 80 nm for references 3 and 4, respectively. Given the thin Si_3N_4 membrane separating the magnetic multilayer from the Au mask, special care has to be taken to prevent altering the magnetic properties of the magnetic system due to Ga^+ ions penetrating through the membrane [5]. The object aperture was fabricated before the magnetic layer deposition to avoid this problem.

This sample–mask structure was placed in the x-ray beam 110 mm downstream of the beamline focus to provide transversely sufficiently coherent illumination, as sketched in figure 1(a). A longitudinal coherence length of $2400\,\lambda = 50\,\mu$m was provided by adjusting the beamline monochromator accordingly. This value exceeds the maximum path length difference

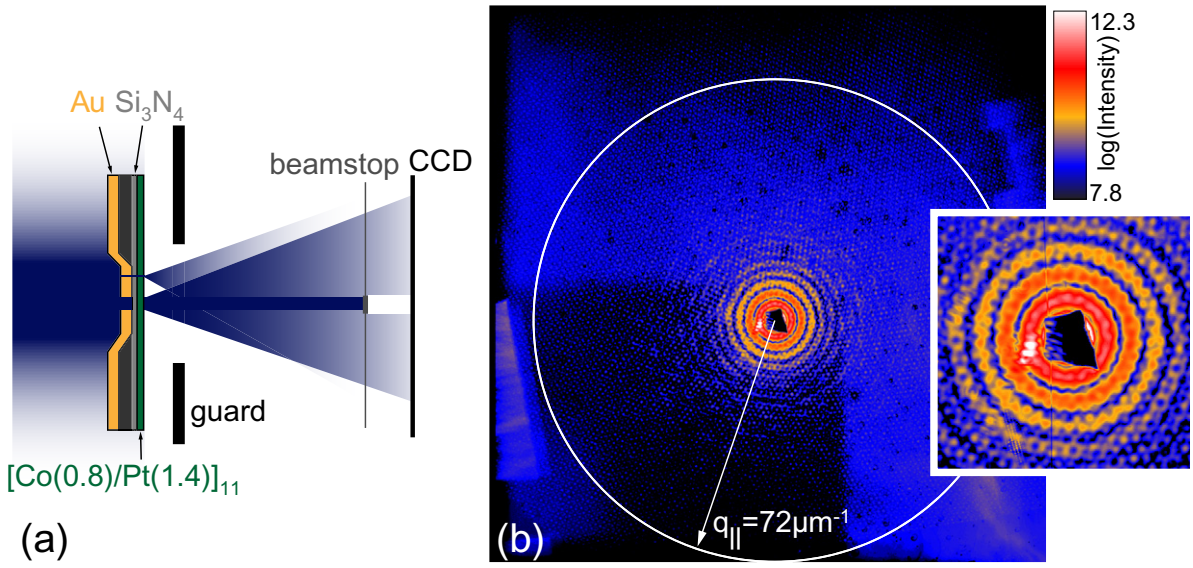

Figure 1. (a) Scheme of the sample and holography experiment. The guard serves to block stray light while the beamstop covers the directly transmitted beam and the Airy disk of the object aperture. (b) Raw-data image of a single photon helicity in a logarithmic scale. Data ranges up to the edges of the CCD while a variety of artifacts can be identified: dirt on the CCD chip (black spots), diffuse stray light bypassing the sample holder and guard aperture (left side and right bottom corner). The left bottom quadrant is shadowed by the sample holder and thus almost free of stray light. The inset is a magnification of the central region.

of 11 μm in our sample, allowing for coherent scattering to all angles. An additional guard aperture (diameter 1.5 mm) against diffuse stray light bypassing the sample holder was placed directly behind our sample.

A 27.6 × 27.6 mm^2 large in-vacuum, back-illuminated CCD detector (2048 × 2048 pixels) was placed 49 mm downstream of the sample to record the interference pattern generated from the object and reference waves. For more details concerning the connection between reciprocal space and resolution in FTH we refer to [19].

3. Results and discussion

A hologram for a single incident x-ray polarization is presented in figure 1(b). The logarithmic intensity scale and chosen colormap serve to emphasize the low-intensity image artifacts such as produced by residual stray light and dust particles on the CCD chip. A beamstop mounted in front of the CCD is blocking the highly intense central part of the hologram, i.e. the unscattered beam and the Airy disc of the object aperture. As we will see below, robust high-quality imaging is possible from raw data containing such artefacts due to the fact that the low-frequency background does not disturb the holographic image reconstruction. We recorded two holograms with opposite helicities (σ^+ and σ^-) of the incident radiation in order to image the magnetic sample features while suppressing non-magnetic contributions [25]. This difference procedure also improves the reconstruction quality with respect to time and

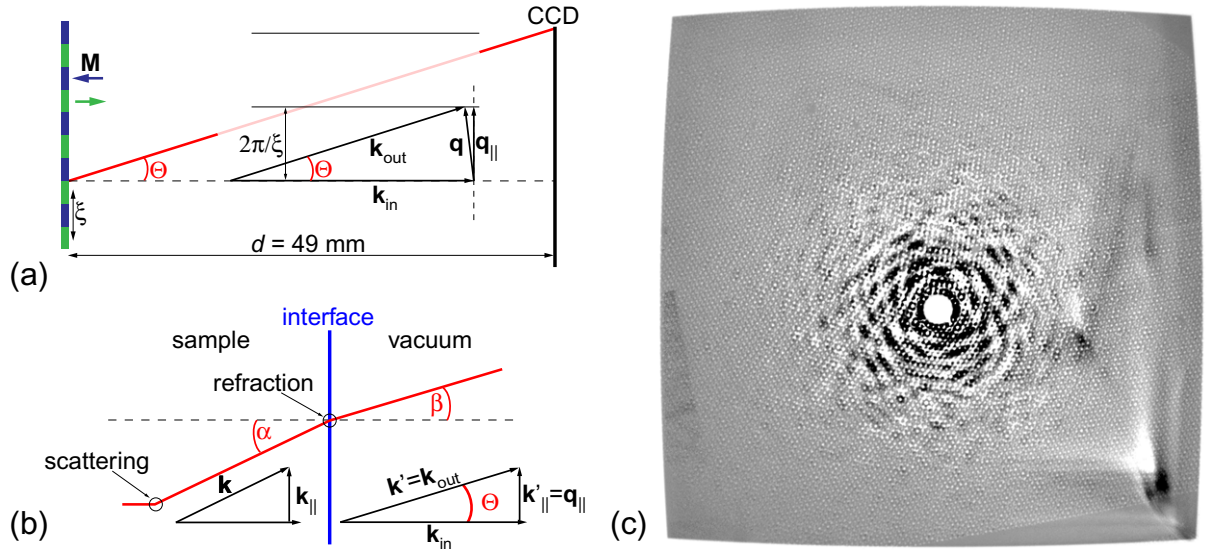

Figure 2. (a) Sketch of the scattering geometry for a thin magnetic-domain sample with a periodicity ξ resulting in elongated reflexes with $2\pi/\xi$-spacing in Fourier space. The hologram intensity has to be remapped to true in-plane components. (b) Refraction of the scattered wave at the sample–vacuum interface. Due to the normal-incidence geometry, the angle of refraction β and the scattering angle Θ are identical and $\mathbf{q}_{\parallel}$ is unaffected by refraction. (c) The difference image after projection to in-plane coordinates drawn with a linear intensity scale. The beamstop has been masked.

polarisation independent features and not varying imaging artefacts mentioned above. With a slightly off-centered detector, the largest momentum transfer collected in all directions is 72 μm^{-1}. The object–reference interference fringes have a period of about 13 pixels on the chip.

The elastic scattering geometry is sketched in figure 2(a). Due to the maximum detected scattering angle of 23.3°, a small-angle approximation is not valid. The necessary projection of the intensity detected by the planar CCD-chip on a sphere of constant absolute momentum transfer in reciprocal space is accomplished by an inverse gnomonic projection. Such a projection has been already reported in [18] for a binary transmission sample. However, for a quasi-2D sample as magnetic domains in a thin magnetic film, the spatial frequencies generating momentum transfer are purely in-plane. A real-space domain periodicity ξ translates to $2\pi/\xi$-spaced reflexes in transverse reciprocal space, with elongation in the longitudinal reciprocal space direction analogous to the crystal truncation rods in surface diffraction [26]. Consequentially, only the in-plane component $\mathbf{q}_{\parallel}$ of the scattering vector yields the correct scaling and has to be considered for image formation. An inverse gnomonic projection alone is insufficient for this task.

In the numerical implementation of the rescaling to $\mathbf{q}_{\parallel}$-coordinates, the measured scattering intensities per solid angle have to be conserved. The projected pixel intensities correspond to the area covered in the detected image, a procedure referred to as exact area imaging. With our algorithm the intensity before and after the projection deviates by less than 0.1%. The mapping of the helicity difference intensity $(I(\sigma^+) - I(\sigma^-))$ to true in-plane Fourier coordinates

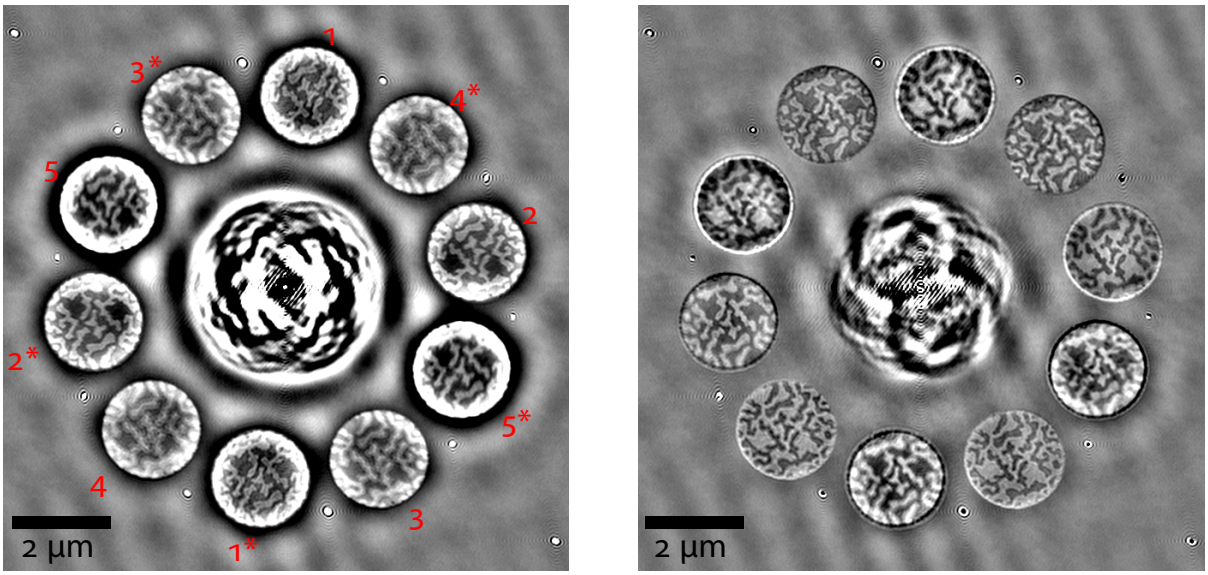

Figure 3. Real part (left) and imaginary part (right) of the object reconstruction from the difference image after projection and sub-pixel accuracy hologram centering. The reconstructions labelled 1, 2 and 5 correspond to the smaller, 60 nm references and 3 and 4 to 80 nm reference apertures. The complex conjugate reconstructions, denoted with *, are centrosymmetric duplicates and contrast inverted for the imaginary part. The strong signal in the latter corresponds to enhanced phase contrast due to non-vanishing $\Delta\delta$. The linear intensity scale is ranging from -7×10^6 to 7×10^6 arb. units.

is presented in figure 2(c). The image edges now feature a slight curvature and the projected pixel area covered in the detected image increases nonlinearly with respect to the distance of the pixel to the optical axis. The beamstop in the center has been masked by a circle blurred with a Gaussian function.

In the vacuum ultraviolet spectral range, the real part of the refractive index is usually significantly deviating from unity. Hence, an influence on the hologram by the refraction of the scattered radiation at the sample interfaces has to be considered in general. At a planar interface between two media, a wave with incident wave vector $\mathbf{k}$ and incident angle α with respect to the sample surface normal will propagate with $\mathbf{k}'$ and angle β in the second medium. Due to boundary conditions the components parallel to the interface $\mathbf{k}_\parallel$ and $\mathbf{k}'_\parallel$ have to be equal, leading to an alternative notation of Snell's law: $|\mathbf{k}| \sin\alpha = |\mathbf{k}'| \sin\beta$. The refracted wave vector $\mathbf{k}'$ is coincident with the scattering vector $\mathbf{k}_{\mathrm{out}}$ and according to the normal incidence geometry in our experiment, the angle of refraction is identical to the scattering angle $\beta = \Theta$. Thus, the $\mathbf{q}_\parallel$-component of the detected scattering vector is not affected by refraction. As a result, the projection to in-plane Fourier coordinates of the scattering vector outlined above, already takes care of refraction corrections in the case of a normal-incidence geometry.

The final reconstruction from the difference hologram corrected to $\mathbf{q}_\parallel$-space is shown in figure 3 with the real and imaginary part. The hologram was centered with subpixel resolution by multiplying the complex reconstruction matrix with a plane wave [5]. A reconstruction of the object region and the complex conjugate twin image (denoted with an asterisk) is clearly visible,

each pair generated by one of the five references. These holographic reconstructions are located around the object autocorrelation in the image center. Note that hardly any ringing artifacts are visible at sharp features such as the object aperture. The bright dots between the object reconstructions arising from reference–reference correlations are particularly good indicators in this respect. Missing or inadequate $\mathbf{q}_{\parallel}$-projection will result in ringing features in addition to deteriorating the reconstruction quality in the field of view within the object aperture.

The black and white areas in the circular field of view represent magnetic domains with an orientation of the magnetization $\mathbf{M}$ to be either parallel or antiparallel to the sample normal. The magnetic domain pattern manifests itself in the real as well as in the imaginary part of the reconstruction. The real part is centrosymmetric, with all object reconstructions and twin images showing positive or negative intensity in the same regions respectively. As expected, the imaginary part shows a contrast inversion for the complex conjugate twin images.

In fact, the image contrast observed in the imaginary part is stronger as compared to the real part, indicating a significant phase shifting fraction of the refractive index [4]. The observed ratio of the magnetic contrast in the real and imaginary part is in line with measurements of the magneto-optical constants $\Delta\beta$, $\Delta\delta$ at the 3p levels of cobalt [22]. As pointed out in [4] for holography at the L-edge energies, it might be advantageous to exploit phase contrast imaging by tuning the photon energy below the absorption resonance to avoid strong beam attenuation. This advantage will be even bigger at M-edge energies due to enhanced absorption in the sample.

Each of the five image reconstructions allows for an unambiguous determination of the domain pattern with up or down magnetized regions. From the line scan presented in figure 4(c) we estimate the spatial resolution to be better than 70 nm. Given the fact, that on one hand slight high pass-filtering is present due to the use of a central beamstop and that the domain walls between up and down magnetized domains can be expected to be several nanometers in width, a more precise determination of the spatial resolution is difficult. We note however, that very narrow domains appearing with a width of about 60 nm in the reconstruction can be resolved (arrow in figure 4(b)).

For the purposes of *destructive* single-shot imaging at FEL sources, one has to consider the achievable image quality from a *single* helicity image as shown in figure 4(b). In contrast to the difference hologram procedure, a CCD dark file was now subtracted. Strong intensity modulations around the autocorrelation in the center of the reconstruction required a flattening of the whole hologram with a two-dimensional Gaussian function of 11 μm^{-1} width.

The information from the real and imaginary parts for one individual reconstruction can be merged by rotating the complex values to the real axis. A complex rotation by 46° and 25° applied to the reconstructions shown in figures 4(a) and (b) respectively, maximized the contrast in this fashion. The blue (a) and red (b) line mark the position of a line scan plotted in figure 4(c) to illustrate the spatial resolution for the difference and single-helicity image. The largest scattering angle recorded in every direction around the optical axis (white circle in figure 1(b)) translates into a resolution of 87 nm. In addition higher momentum transfer data is recorded outside of this circle on the CCD, with the largest scattering angle of 23.3° corresponding to a diffraction-limited resolution of 51 nm. As we clearly resolve the width of single magnetic domains including the particularly narrow domain marked by the arrow in figure 3(b) we determine our resolution to be at least 70 nm also in the single-helicity case of relevance for single-shot imaging at FELs.

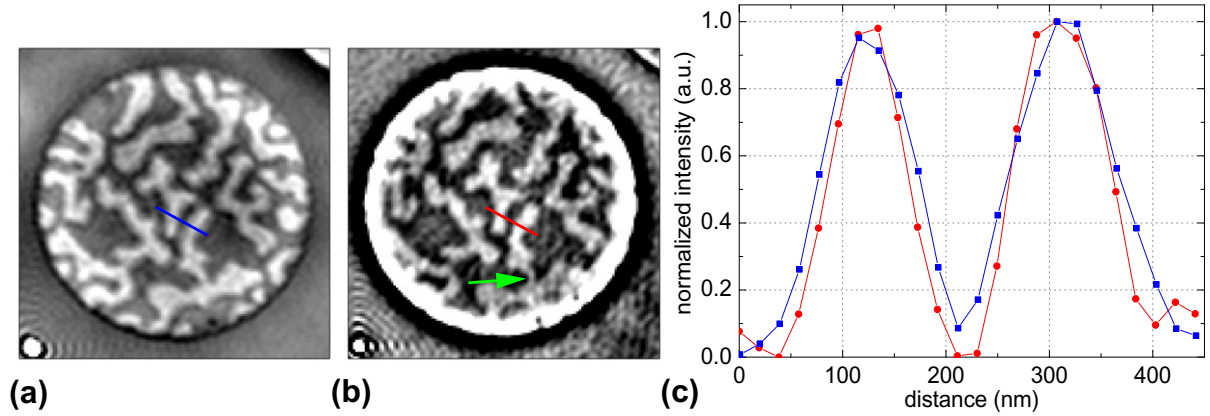

Figure 4. (a) Real part of the difference image reconstruction from reference 3 and (b) single circular polarization image reconstruction from reference 5 plotted in a linear scale. In (a) and (b) the complex values have been rotated to the real part. The intensity scales linearly from -7×10^6 to 7×10^6 arb. units for both images. The blue and red lines indicate the corresponding sections plotted in (c). The sampling distance is 18.4 nm after zero-padding the hologram matrix to 4096×4096 pixels.

From beamline parameters and the acceptance angle of our holographic mask downstream of the beamline focus, we estimate a total x-ray dose of 4×10^{10} photons μm^{-2} during the exposure time. Given an FEL output of about 10^{12} photons per pulse, it should be possible to record a hologram with comparable image statistics in one *single shot* at an FEL. Here, no transverse coherence filtering is required and the natural bandwidth is sufficient for resonant scattering at the M-edges of 3d transition metals. We note, however, that circularly polarized radiation is necessary to image domains magnetized along the direction of the beam. While this is not an issue for FELs with elliptical undulators [27], the additional polarizer required at FELs with planar undulators or typical HHG sources will lead to a reduction of the incident photon flux for such sample systems [28, 29]. As x-ray FELs operating with intrinsically circularly polarized radiation currently do reach wavelengths corresponding to the 3d transition metal M-edges while the respective L-edges are yet inaccessible, our results on M-edge FTH imaging may be considered of particular interest. Nonlinear effects leading to a breakdown of the resonant scattering cross-section, as reported recently [30], may potentially be mitigated in the attosecond regime accessible by HHG sources and possibly by FELs in the future [31, 32].

4. Conclusion

In conclusion we have demonstrated FTH in the 60 eV wavelength regime with equal quality to images recorded at the transition metal L-edges around 780 eV. To obtain high-quality images of two dimensional samples such as magnetic thin films, it is crucial to transform the measured intensity pattern into a hologram in $\mathbf{q}_\parallel$-coordinates. This procedure does not only correct for Ewald's sphere curvature, but at the same time accounts for refraction effects in normal-incidence geometry. High-quality images are also obtainable with a single-helicity

measurement, allowing for single-shot experiments. We achieved a diffraction-limited resolution below 70 nm and expect future experiments at FEL or HHG sources operating in this wavelength regime to be able to take advantage of this approach in order to combine sub-100 nm spatial resolution with sub-picosecond temporal resolution.

Acknowledgments

We acknowledge support from the Bundesministerium für Bildung und Forschung under contract no. 05K10KTB/FSP-301 ('MPScatt').

References

[1] McNulty I, Kirz J, Jacobsen C, Anderson E H, Howells M R and Kern D P 1992 *Science* **256** 1009–12
[2] Eisebitt S, Lörgen M, Eberhardt W, Lüning J, Andrews S and Stöhr J 2004 *Appl. Phys. Lett.* **84** 3373
[3] Günther C M, Radu F, Menzel A, Eisebitt S, Schlotter W F, Rick R, Lüning J and Hellwig O 2008 *Appl. Phys. Lett.* **93** 72505
[4] Scherz A *et al* 2007 *Phys. Rev.* B **76** 214410
[5] Streit-Nierobisch S *et al* 2009 *J. Appl. Phys.* **106** 83909
[6] Pfau B *et al* 2011 *Appl. Phys. Lett.* **99** 62502
[7] Günther C M *et al* 2010 *Phys. Rev.* B **81** 64411
[8] Beaurepaire E, Merle J C, Daunois A and Bigot J Y 1996 *Phys. Rev. Lett.* **76** 4250–3
[9] Stanciu C, Hansteen F, Kimel A, Kirilyuk A, Tsukamoto A, Itoh A and Rasing T 2007 *Phys. Rev. Lett.* **99** 047601
[10] Ostler T A *et al* 2012 *Nature Commun.* **3** 666
[11] Koopmans B, Malinowski G, Dalla Longa F, Steiauf D, Fähnle M, Roth T, Cinchetti M and Aeschlimann M 2010 *Nature Mater.* **9** 259–65
[12] Rudolf D *et al* 2012 *Nature Commun.* **3** 1037
[13] Turgut E *et al* 2013 *Phys. Rev. Lett.* **110** 197201
[14] Graves C E *et al* 2013 *Nature Mater.* **12** 293–8
[15] Malinowski G, Dalla Longa F, Rietjens J H H, Paluskar P V, Huijink R, Swagten H J M and Koopmans B 2008 *Nature Phys.* **4** 855–8
[16] Pfau B *et al* 2012 *Nature Commun.* **3** 1100
[17] Vodungbo B *et al* 2012 *Nature Commun.* **3** 999
[18] Sandberg R L, Raymondson D A, La-O-Vorakiat C, Paul A, Raines K S, Miao J, Murnane M M, Kapteyn H C and Schlotter W F 2009 *Opt. Lett.* **34** 1618–20
[19] Pfau B *et al* 2010 *New J. Phys.* **12** 095006
[20] Wang T *et al* 2012 *Phys. Rev. Lett.* **108** 267403
[21] Eisebitt S, Lüning J, Schlotter W F, Lörgen M, Hellwig O, Eberhardt W and Stöhr J 2004 *Nature* **432** 885–8
[22] Valencia S, Gaupp A, Gudat W, Mertins H C, Oppeneer P M, Abramsohn D and Schneider C M 2006 *New J. Phys.* **8** 254
[23] Hubert A and Schäfer R 1998 *Magnetic Domains* 3rd edn (Heidelberg: Springer)
[24] Schlotter W F *et al* 2006 *Appl. Phys. Lett.* **89** 163112
[25] Eisebitt S, Lörgen M, Eberhardt W, Lüning J, Stöhr J, Rettner C, Hellwig O, Fullerton E and Denbeaux G 2003 *Phys. Rev.* B **68** 104419
[26] Stangl J, Holý V and Bauer G 2004 *Rev. Mod. Phys.* **76** 725–83
[27] Capotondi F *et al* 2013 *Rev. Sci. Instrum.* **84** 051301

[28] Vodungbo B *et al* 2011 *Opt. Express* **19** 4346
[29] Pfau B, Günther C M, Koennecke R, Guehrs E, Hellwig O, Schlotter W F and Eisebitt S 2010 *Opt. Express* **18** 13608–15
[30] Müller L *et al* 2013 *Phys. Rev. Lett.* **110** 234801
[31] Emma P, Bane K, Cornacchia M, Huang Z, Schlarb H, Stupakov G and Walz D 2004 *Phys. Rev. Lett.* **92** 074801
[32] Rosenzweig J *et al* 2008 *Nucl. Instrum. Methods Phys. Res.* A **593** 39–44